Available online at www.sciencedirect.com
ScienceDirect
Trans. Nonferrous Met. Soc. China 35(2025) 3919−3932
Transactions of Nonferrous Metals Society of China
www.tnmsc.cn

Alloying process of Mg−La in NaCl−KCl−$MgCl_2$−$LaCl_3$ melts

Jia ZHAO[1,2], Zhi-tao SONG[1,2], Gui-min LU[1,2]

1. National Engineering Research Center for Integrated Utilization of Salt Lake Resources, East China University of Science and Technology, Shanghai 200237, China;
2. Joint International Laboratory for Potassium and Lithium Strategic Resources, East China University of Science and Technology, Shanghai 200237, China

Received 5 March 2024; accepted 10 December 2024

Abstract: The alloying process of Mg−La in NaCl−KCl−$MgCl_2$−$LaCl_3$ (NKML) melts during electroreduction was elucidated using electrochemical techniques and deep potential molecular dynamics (DPMD) simulations. In the NKML system, the Mg^{2+}/La^{3+} electrodeposition on the tungsten (W) electrode at 973 K was found to be a one-step process. The nucleation of metal ions on the electrode surface followed an instantaneous nucleation mode and was not influenced by the alloying process. The redox potential and underpotential deposition behavior of the metal ions in the NKML system were accurately predicted by the DPMD simulations, confirming the alloying process of the Mg−La. Additionally, scanning electron microscopy with energy dispersive spectroscopy (SEM−EDS) analysis results confirmed that the cathodic deposits consisted of a bright phase and a dark phase, corresponding to the Mg−La alloys and Mg, respectively. The distribution of electrolytic products suggests that the cathodic deposit initially favors the Mg phase, with the Mg−La alloy forming more easily when the Mg source in the melt is depleted.

Key words: NaCl−KCl−$MgCl_2$−$LaCl_3$ melt; Mg−La alloy; alloying process; electroreduction; redox potential

1 Introduction

Lanthanum (La) has been shown to have a beneficial effect on magnesium (Mg) alloys by regulating grain growth, increasing corrosion resistance [1], and improving mechanical properties [2]. These advances elevate the performance of Mg alloys and promote their broader application in the automotive [3], electronics 3C [4], and aerospace industries [5].

Molten salt electrolysis, which has emerged as the preferred method for alloy production, is highly attractive due to its advantages, such as easy control of product composition, homogeneous distribution without segregation, and low energy consumption [6,7]. Recently, several studies have investigated the electrochemical processes involved in producing Mg-based alloys through molten salt electrolysis [8−12]. In the case of Mg−La alloys, WANG et al [8] observed the underpotential deposition behavior of La^{3+} on a Mg substrate in LiCl−KCl melt. JI et al [9] employed potentiostatic and galvanostatic electrolysis to synthesize Mg−La compounds and Mg−Li−La alloys, respectively. SAHOO et al [10] produced Mg−La alloys via co-electrodeposition in $MgCl_2$−$LaCl_3$−KCl melt, and by adjusting the $MgCl_2$ and $LaCl_3$ contents in the melt, and they achieved phase regulation of electrolysis products, including MgLa, MgLa+ Mg_2La, Mg_2La, and $Mg_{17}La_2$. In a similar system, WANG et al [11] discovered that the current decreases as the $LaCl_3$ concentration increases. TAKENAKA et al [12] prepared La-containing Mg alloys in a NaCl−KCl−$MgCl_2$−$LaCl_3$ (NKML) system by direct electrodeposition, demonstrating

Corresponding author: Gui-min LU, Tel: +86-21-64252173, E-mail: gmlu@ecust.edu.cn
https://doi.org/10.1016/S1003-6326(25)66921-4

that the La content in the product depends on both the $LaCl_3$ concentration in the melt and the applied cathodic voltage. The corrosion testing revealed that the corrosion resistance of Mg−La alloys produced by molten salt electrolysis was superior to that of pure Mg.

Mg−La alloys have been investigated in various molten salt systems. Among these, LiCl is not suitable as an additive due to its high cost in practical production; furthermore, conducting electrochemical experimental studies using KCl alone as a supporting electrolyte presents challenges. The use of NaCl−KCl as a supporting electrolyte is both cost-effective and feasible at an acceptable operating temperature. Additionally, NaCl−KCl−$MgCl_2$ is a common electrolyte formulation used in magnesium electrolysis, making the NKML melt compatible with the existing magnesium electrolysis process, which enhances its potential for industrial promotion and application. Therefore, studying the alloying process of Mg−La in the NKML system is of significant importance. Although similar studies exist, the mechanism of Mg−La alloy electro-reduction in NKML melts has yet to be thoroughly explored. Moreover, the existing literature rarely emphasizes the alloying process during electro-reduction.

In recent years, deep potential molecular dynamics (DPMD) simulations, which utilize machine learning, have emerged as a novel technique in the field of molten salts. This method has been applied to analyzing the microstructure and thermodynamic properties of molten salts [13,14], as well as the redox potentials of metal ions in melts [15]. Building on our previous study [16], in this work, the alloying process of Mg−La in the NKML system during electroreduction was investigated through a combination of electrochemical experiments and DPMD simulations. Additionally, the deposition process was examined based on the microstructural characterization of the Mg−La alloy.

2 Methodology

2.1 Electrochemical experiments

The entire salt mixture was vacuum-dried at 473 K for 20 h and subsequently stored in a glove box (Microuna) to maintain O_2 and H_2O contents below 0.1×10^{-6} (mass fraction). For each experiment, the eutectic composition of NaCl (Aladdin, >99.5%) and KCl (Aladdin, >99.5%) supplied by Shanghai Aladdin Biochemical Technology Co. was used. Anhydrous $MgCl_2$ (Macklin, >99.5%) and $LaCl_3$ (Macklin, >99.5%) were provided by Shanghai Zhonghe Chemical Technology Co. as sources of Mg^{2+} and La^{3+}. To eliminate potential impurities, the potentiostatic method was applied at −1.70 V (vs Ag/AgCl) for 2 h prior to electrolysis. The salts for electrochemical experiments were melted in a sealed resistance furnace, with a continuous supply of argon gas (>99.99%) ensuring the inert atmosphere. All electrochemical measurements were conducted using an electrochemical workstation (Princeton 4000) with a three-electrode system. A tungsten rod (diameter d=1 mm) served as the working electrode, while a spectrally pure graphite rod (d=6 mm) was used as the auxiliary electrode. A self-made Ag/AgCl reference electrode, composed of a silver wire embedded in a NaCl−KCl−AgCl mixture (1 wt.%), was employed. Unless otherwise specified, the effective surface area of the working electrode for electrochemical experiments was 0.322 cm^2.

2.2 Computational details

Six different compositions were developed to predict the redox potentials of Mg^{2+} and La^{3+} ions in NaCl−KCl melts. Detailed information regarding the number of atoms and ions in both the oxidized (-ox) and reduced (-red) states is provided in Table 1. In all cases, the reduced states were derived from the oxidized states by reducing the Cl^- balance. This approach has been previously employed to predict redox potentials in other molten salt systems [17,18]. The presence of Mg^{2+} in the melt induces the deposition of La^{3+} at lower potentials during the reduction process, providing compelling evidence for the Mg−La alloying phenomenon in the melt. To further explore this process, La(Mg)-ox and La(Mg)-red states were developed, with (Mg) representing the metal Mg previously deposited on the electrode surface.

The schematic diagram for calculating the thermodynamic behavior is shown in Fig. 1. In this study, ab initio molecular dynamics (AIMD) simulations were conducted using the Vienna Ab initio Simulation Package (VASP) [19]. AIMD simulations for each system were carried out for

Table 1 Numbers (N) of different metal atoms and ions in ox- and red-states for calculating redox potential in NaCl−KCl melts

System	$N(Na^+)$	$N(K^+)$	$N(Mg^{2+})$	$N(La^{3+})$	$N(Cl^-)$	N(Mg)	N(La)
Mg-ox	20	20	2	2	50	0	0
Mg-red	20	20	1	2	48	1	0
La-ox	20	20	0	2	46	0	0
La-red	20	20	0	1	43	0	1
La(Mg)-ox	20	20	0	2	46	1	0
La(Mg)-red	20	20	0	1	43	1	1

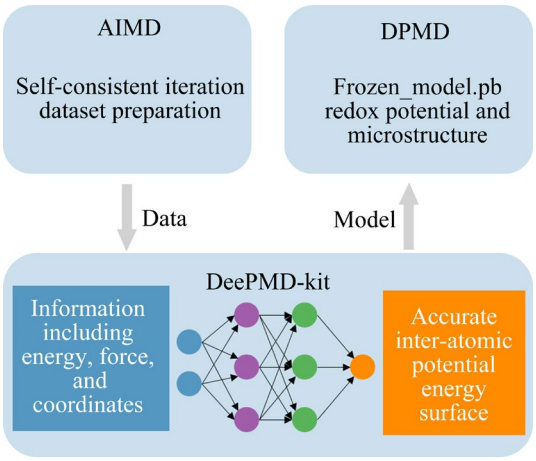

Fig. 1 Schematic representation of calculation method for predicting thermodynamic behavior of NKML melts

10 ps at 973 K, with the input parameters for VASP kept consistent with those in our previous work [16]. Data from the AIMD simulations, including energy, force, and coordinates, were collected to serve as the initial data set. The exact interatomic potential surface was then generated using a machine learning approach, implemented through the DeePMD kit package [20].

The deep potential (DP) model was trained for 5×10^5 steps, with embedding and adapting networks consisting of three layers. The initial and final prefactors for energy and force were set to (0.02, 1) and (1000, 1), respectively. DPMD simulations were conducted using the Large-scale Atomic/Molecular Massively Parallel Simulator (LAMMPS) [21], which was compiled with the DP module to analyze the thermodynamic behavior of the NKML melts. Each system was first simulated in a 500 ps NPT ensemble, followed by 500 ps simulations in the NVT ensemble.

2.3 Electrolysis and Mg−La alloy characterization

The Mg−La alloy was produced using the potentiostatic method at 973 K. After electrolysis, the alloy was cooled in an argon atmosphere in the furnace before being mechanically extracted from the salt. The alloy was then cleaned with anhydrous ethanol (99.5%, Macklin) using ultrasonic waves to remove any residual salts. Subsequently, it was processed using an automatic grinding and polishing machine (MECATECH 234, PRESI, France) in preparation for microstructural analysis. Specifically, the samples were embedded, ground (75, 40, and 20 μm), and polished (9, 3, and 1 μm).

The microstructure of the alloy was observed using a scanning electron microscope (S−3400N, Hitachi, Japan), and microzone analysis was simultaneously conducted with an energy dispersive X-ray spectroscope (Falion 60S, EDAX, USA). The crystal phases of the alloys were identified using an X-ray powder diffractometer (D/Max 2550 VB/PC, Rigaku, Japan) within a 2θ range of 10°−80°, with increments of 0.02°, employing monochromatic Cu K_α radiation (40 kV, 100 mA). The elemental composition of the alloy products was quantified using an optical emission spectrometer with inductively coupled plasma (ARCOS FHS12, Spectro, Germany).

3 Results and discussion

3.1 Electroreduction results

3.1.1 Cyclic voltammetry analysis results

Figure 2 presents the cyclic voltammogram (CV) curves obtained on a tungsten electrode for different systems at 973 K. The green curve represents the typical CV result for the NaCl−KCl melt, showing a distinct redox peak E/E' (−2.01 V/−1.79 V) in the negative potential region, corresponding to the deposition and dissolution of Na, respectively. After introducing 2 wt.% $LaCl_3$ into the NaCl−KCl system (orange curve), the cathodic current at −1.77 V increased significantly

compared to that of the NaCl−KCl system. This is due to the deposition potential of La being close to that of Na, resulting in the current being a combined contribution from the formation of both La and Na. Additionally, a clear oxidation signal *D′* was observed during the anodic scan, corresponding to the oxidation of La deposited on the electrode surface. Simultaneously, the intensity of *E′* weakened considerably, as part of the current was consumed by La reduction during the cathodic scan.

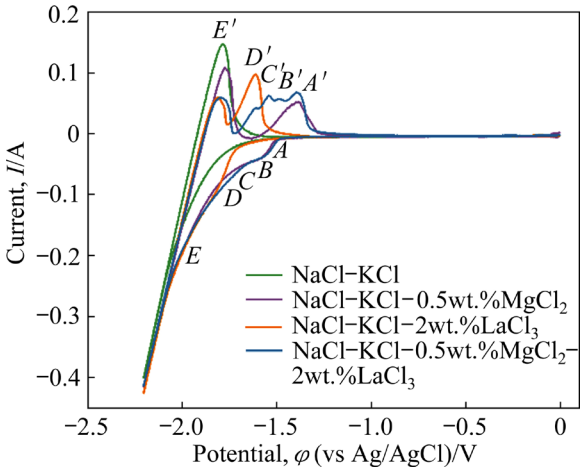

Fig. 2 CV curves for various systems at 973 K with scan rate of 0.1 V/s

For the NaCl−KCl−0.5wt.%$MgCl_2$ system (purple curve), the CV curve revealed a new anodic signal, *A′*, adjacent to *E*/*E′*, which was attributed to Mg dissolution. The current onset shifted to approximately −1.49 V, corresponding to the deposition potential of Mg in the NaCl−KCl melt. When 0.5 wt.% $MgCl_2$ and 2 wt.% $LaCl_3$ were simultaneously added to the NaCl−KCl system, the CV produced a sky-blue curve. In the anodic direction, in addition to the oxidation peaks *A′*, *B′*, and *C′*, two new anodic signals, *D′* and *E′*, appeared, which were associated with the formation of the Mg−La alloy during the electroreduction process. This behavior is consistent with previous CV analyses of Mg−Nd [22] and Mg−Tm [23] alloys. The phase diagram of the Mg−La alloy [24] indicates the presence of two solid intermetallic compounds, Mg_3La and MgLa, at 973 K, corresponding to *B′* and *C′*, respectively.

The deposition signal of the alloy lies between those of the two pure metals. To distinguish the electrochemical signals generated by the deposition of Mg−La alloys, different cathodic potentials were applied, covering the potential range from −1.60 to −1.80 V, as shown in Fig. 3. When the potential is set to −1.60 V, the electrochemical window shows only a pair of redox peaks corresponding to the deposition and redox formation of Mg. When the cathodic potential is shifted to −1.70 V, the *B′* peak is observed, while at −1.75 V, the *C′* peak becomes visible. When the cathodic reversal is shifted to −1.80 V, the signal of La oxidation appears during the positive-going scan. Consequently, the deposition potentials of Mg_3La, MgLa, and La in the NKML system on the tungsten electrode are −1.67, −1.71, and −1.77 V, respectively. By adjusting the termination potential from −1.90 to −2.20 V, the dissolution signal of Na (*E′*) was detected during the anodic scan, and the deposition potential of Na was determined to be −2.01 V.

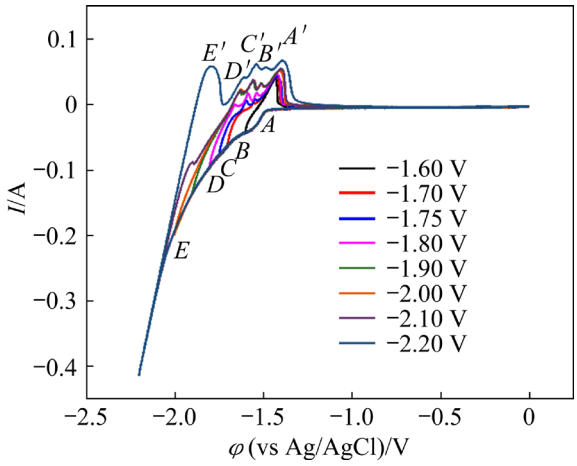

Fig. 3 CV curves at different potential windows for NaCl−KCl−0.5wt.%$MgCl_2$−2wt.%$LaCl_3$ system at 973 K

3.1.2 Square-wave voltammetry analysis results

Square-wave voltammetry (SWV) has proven to be a more sensitive electrochemical technique than CV and is therefore frequently used to investigate the electroreduction mechanisms of metal ions in molten salts [25]. Figure 4 presents the results of SWV analysis for different melts, with a pulse height of 25 mV, a step potential of 2 mV, and a frequency of 10 Hz. Compared to the CV curves in Fig. 2, clear reduction signals were observed in the SWV. In the NKML system, four reduction signals were detected. When compared with the NaCl−KCl system, signal *E* was identified as the Na reduction signal. Similarly, peaks *A* and *D* were associated with the reduction of Mg^{2+} and La^{3+} on the electrode surface, respectively. Additionally, a clear reduction signal was observed between *A*

and *D*, which corresponded to the formation of the Mg−La alloy. The positive-going scanning process (i.e., square-wave dissolution voltammetry) for the NKML system was then examined, and five anodic peaks were identified. Peaks *B′* and *C′* represent the dissolution of Mg as Mg^{2+} along with the dissolution of Mg−La compounds. During NKML electroreduction, two alloys were deposited on the surface of the tungsten electrode, with peaks (*B* and *C*) overlapping during reduction due to their close potential values.

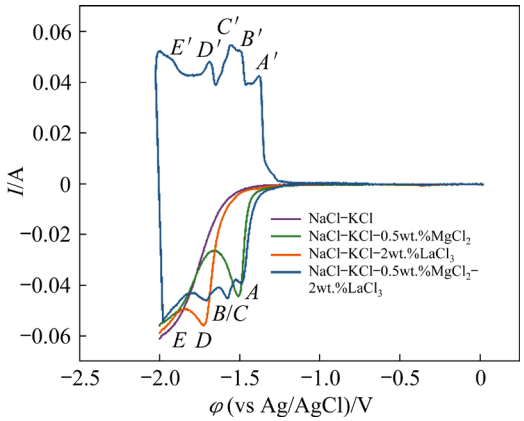

Fig. 4 SWV analysis results for various melts at 973 K

3.1.3 Open-circuit chronopotentiometry analysis results

Open-circuit chronopotentiometry (OCP) is a powerful electrochemical method for studying alloy formation and dissolution. Figure 5 presents the comparative results of potential evolution over time (*t*) in different melts at 973 K. Initially, a constant potential pulse of −2.52 V was applied for 2 s, during which a sample layer was deposited on the working electrode. The potential then increased and reached a plateau, with each plateau indicating the coexistence of two phases.

The sky-blue curve shows potential Plateau 1 at approximately −1.92 V, representing the equilibrium potential of the Na^+/Na pair in the NaCl−KCl system. After $LaCl_3$ was introduced into the NaCl−KCl system (green curve), the potential evolution over time was revealed. In addition to Plateau 1, a potential Plateau 2 at −1.70 V, associated with the equilibrium potential of the La^{3+}/La pair appeared. The appearance of Plateau 5 (−1.48 V) in the NaCl−KCl−0.5wt.%$MgCl_2$ melt corresponds to the Mg^{2+}/Mg pair in the NaCl−KCl system. The orange curve represents the OCP results for the NKML system, where five potential plateaus were observed. Plateaus 1, 2, and 5 correspond to the stripping of Na, La, and Mg, respectively. Plateau 3, at −1.61 V, is attributed to the intermetallic compound MgLa, which contains the highest concentration of La [22]. Plateau 4, at −1.54 V, was determined to represent Mg_3La. The possible equilibrium reactions for these plateaus are expressed in Eqs. (1) and (2). Therefore, Plateaus 3 and 4 are likely to correspond to the coexistence of MgLa and Mg_3La, and Mg_3La and Mg, respectively.

$$\frac{3}{2}MgLa - 3e \rightleftharpoons \frac{1}{2}Mg_3La + La^{3+} \quad (1)$$

$$Mg_3La - 3e \rightleftharpoons 3Mg + La^{3+} \quad (2)$$

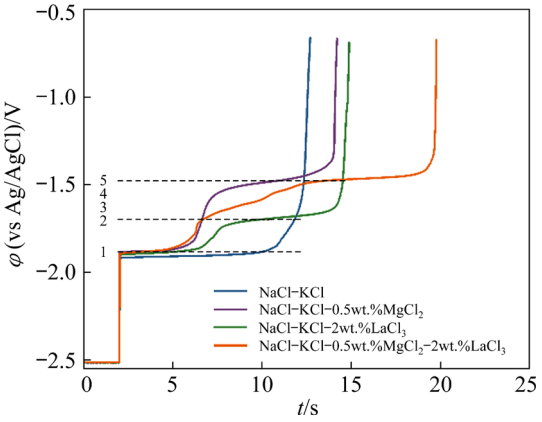

Fig. 5 Comparative results of OPC curves of different melts on tungsten electrodes at 973 K

3.1.4 Chronoamperometry analysis results

Chronoamperometry monitors the current development over time under a constant potential pulse and was employed in this work to investigate the nucleation behavior of metal ions on the electrode surface and their diffusion characteristics in the melt. Figure 6 displays the *I*–*t* curves for various melts at different applied potentials, along with comparative results between the experimental data and theoretical nucleation models. To study the nucleation mechanism of metal ions on the electrode surface, three potential ranges were selected based on the voltammetry results: from −1.60 to −1.66 V, from −1.80 to −1.86 V, and from −1.68 to −1.78 V, respectively. The *I*–*t* curves obtained for all systems can be divided into three phases. The first phase is characterized by a rapid increase in current to its maximum, which corresponds to the nucleation and subsequent growth of the metal. In the second phase, the current

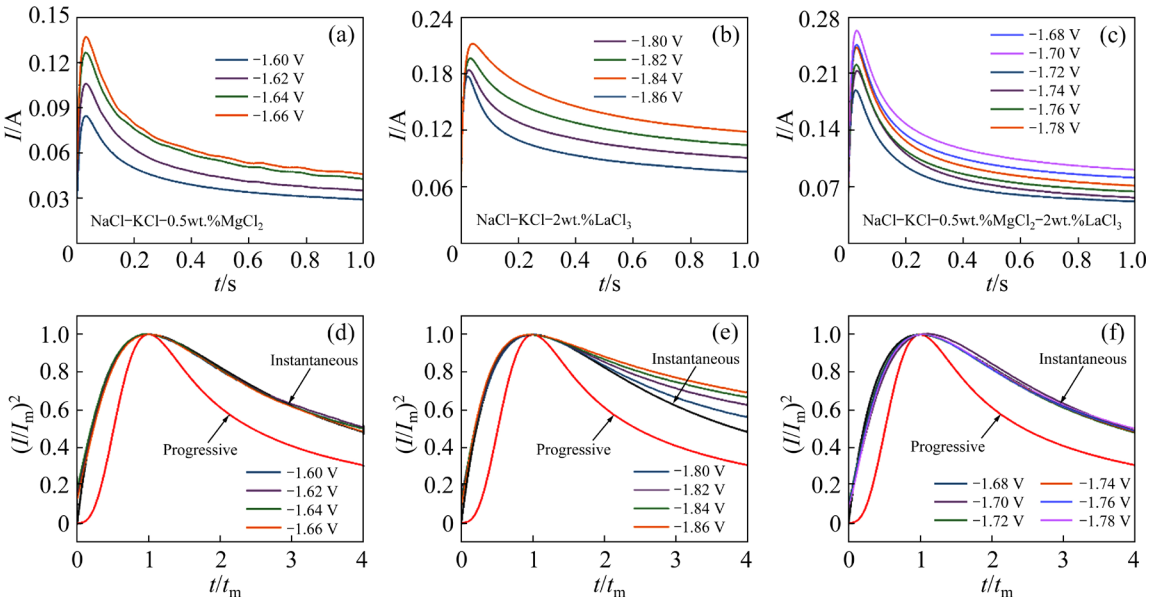

Fig. 6 Chronoamperometric *I*–*t* curves of various melts at different applied potentials and corresponding comparative results

gradually decreases, indicating that ion diffusion controls the process. In the third phase, the current stabilizes as mass transfer and the electrode reaction reach equilibrium.

In this work, the non-dimensional models proposed by SCHARIFKER and HILLS [26] were applied to analyzing the nucleation pattern of metal ions on the tungsten electrode. These models were typically derived from *I*–*t* data, and the corresponding expressions were defined by Eqs. (3) and (4):

For instantaneous nucleation, there exists

$$\left(\frac{I}{I_m}\right)^2 = 1.9542\left(\frac{t_m}{t}\right)\left\{1-\exp\left[-1.2564\left(\frac{t}{t_m}\right)\right]\right\}^2 \quad (3)$$

For progressive nucleation, there exists

$$\left(\frac{I}{I_m}\right)^2 = 1.2254\left(\frac{t_m}{t}\right)\left\{1-\exp\left[-2.3367\left(\frac{t}{t_m}\right)^2\right]\right\}^2 \quad (4)$$

where I is the current, I_m is the peak current, t is the time, and t_m is the time corresponding to the peak current.

Figures 6(d), (e), and (f) show the comparison of the experimental data with the theoretical models for instantaneous and progressive nucleation. According to the results of the CV analysis, Fig. 6(f), corresponding to the deposition of the Mg−La alloy, follows the same nucleation mode as Figs. 6(d) and (e), which are both indicative of instantaneous nucleation. This finding suggests that the nucleation mechanism of the metal ions is not affected by the alloying process in the NKML system.

The linear dependence between I and $t^{-1/2}$, as shown in Figs. 6(a) and (b), is presented in Fig. 7. From this, the diffusion coefficients of Mg^{2+} and La^{3+} in NaCl−KCl were determined to be 2.80×10^{-5} and 0.87×10^{-5} cm^2/s, respectively, using Cottrell's equation as described in Eq. (5):

$$I = \frac{nFAD^{1/2}C_0}{\pi^{1/2}t^{1/2}} \quad (5)$$

where n is the number of the transferred electrons, F is the Faraday constant, A is the area of the working electrode, D is the diffusion coefficient of the ions in the molten salt, C_0 is the mass concentration of Mg^{2+} or La^{3+}, and t is the polarization time.

3.2 DPMD simulations

3.2.1 DP model performance

Before calculating the thermodynamic behavior of the NKML system, the accuracy of the DP model was thoroughly evaluated from multiple perspectives, including the root mean square error (RMSE) of energy and force, the comparison of energy and force data predicted by the DP model

with density functional theory (DFT) results, and the reproducibility of the radial distribution function (RDF). Table 2 presents the RMSE values for energy and force for all designed systems, with the maximum energy error being 1.20 meV/atom and the maximum force error reaching 33.98 meV/Å. The RMSE results for all states are consistent with those reported in Refs. [14,27], demonstrating that the trained DP model is reliable.

A visual comparison of the energy and force predicted by the DP model with the DFT results is shown in Fig. 8. In this figure, the horizontal axis represents the DFT results, while the vertical axis represents the results predicted by the DP model. It is evident that the energy and the x, y, and z components of the force for all states are uniformly distributed along the diagonal. This uniform distribution indicates that the trained DP model successfully achieves DFT-level accuracy in predicting both energy and force.

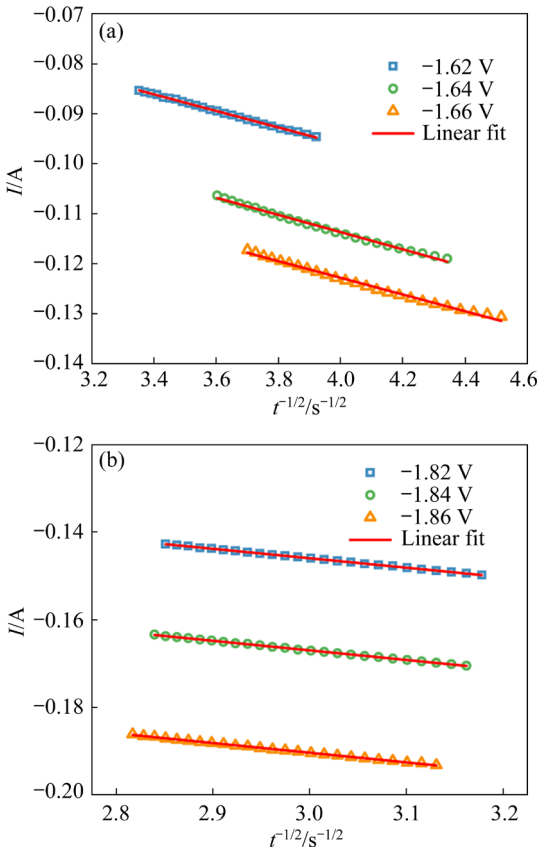

Fig. 7 Linear dependence of I versus $t^{-1/2}$ for NaCl−KCl−0.5wt.%$MgCl_2$ (a) and NaCl−KCl−2wt.%$LaCl_3$ (b) melts at 973 K, with red curves representing fitted results

Table 2 RMSEs of energy and force for designed systems

System	RMSE for energy/(meV·atom^{-1})	RMSE for force/(meV·Å^{-1})
Mg-ox	0.44	23.59
Mg-red	0.32	33.68
La-ox	0.51	25.59
La-red	0.49	33.98
La(Mg)-ox	1.20	33.84
La(Mg)-red	0.59	29.09

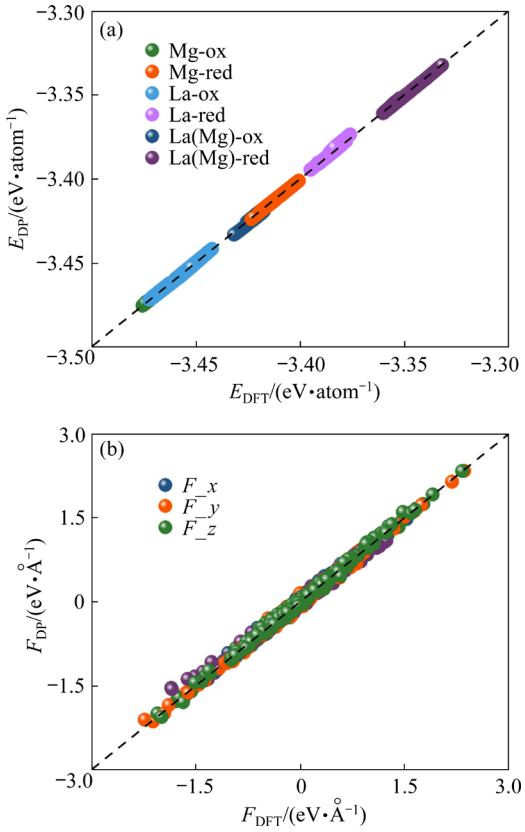

Fig. 8 (a) Energy (E) comparison between DP and DFT results; (b) Force (F) comparison between DP and DFT results

The RDF is an essential tool for characterizing liquid materials. The robustness of the DP model is also demonstrated by its ability to accurately reproduce the RDF, as shown in Fig. 9. Figure 9(a) presents the RDFs for Na−Cl, K−Cl, Mg−Cl, and La−Cl, comparing results from the systems $MgCl_2$−NaCl [28], $MgCl_2$−KCl [29], and $LaCl_3$ [30]. The RDFs obtained from the DPMD simulation align closely with those from the AIMD simulation and reference data, with only a slight difference observed in the height of the first peaks for Mg−Cl and La−Cl. These comparative results confirm that the well-trained DP model delivers sufficient accuracy for further investigations.

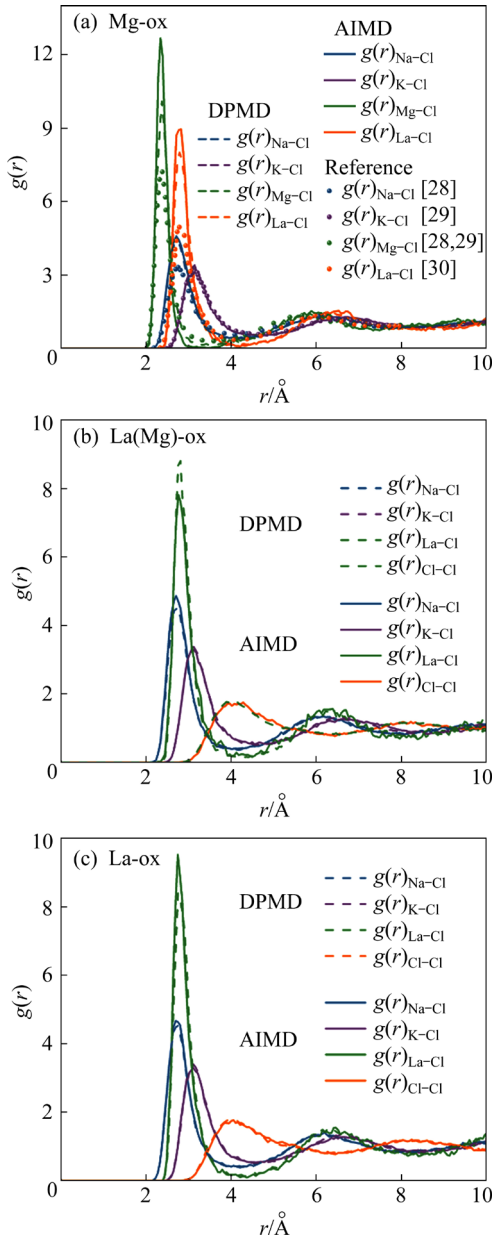

Fig. 9 Radial distribution function ($g(r)$) from DPMD simulation compared to AIMD simulation

3.2.2 Prediction of redox potential

Figure 10 presents the total energy distribution of the NKML melt, which exhibits a high central peak with a symmetrical distribution on both sides. A Gaussian fit was applied to characterizing this energy distribution. The mathematical expectation value was used to approximate the ensemble mean, representing the energy of the system in this state. Based on this approach, the redox potentials of Mg^{2+} and La^{3+} in the NKML system were evaluated following the strategy proposed by NAM and MORGAN [31]. Table 3 shows the mathematical expectation derived from the Gaussian fit and the predicted redox potential.

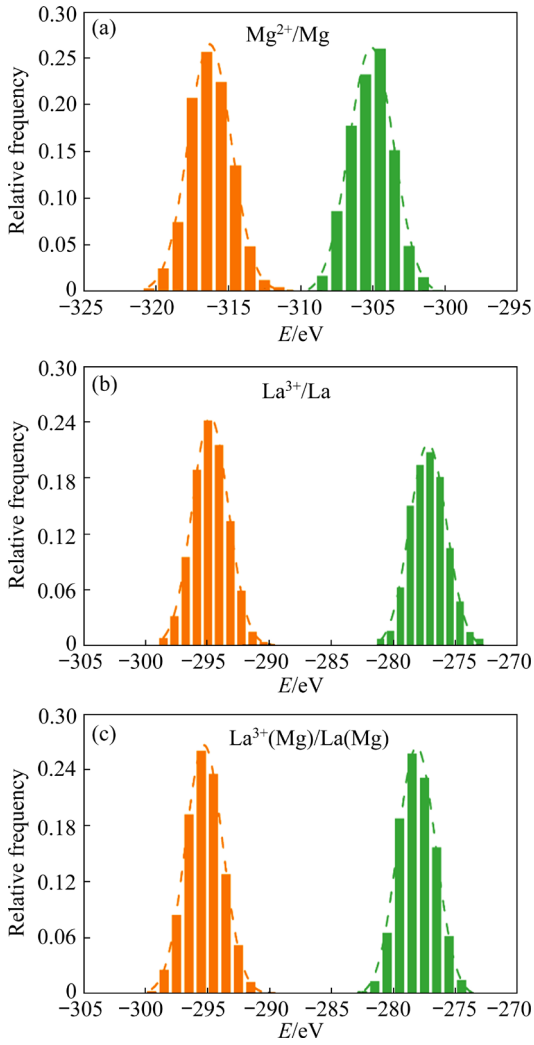

Fig. 10 Total energy distribution and Gaussian fit results for NKML melt at 973 K

For the Ag/AgCl reference electrode, which contains a low AgCl concentration, the electrode potential between it and Cl_2/Cl^- can be expressed mathematically:

$$\varphi_{Ag/AgCl}\ (\text{vs}\ Cl_2/Cl^-)=-1.0910+1.17\times10^{-5}T \quad (6)$$

where T is the thermodynamic temperature.

The redox potentials relative to Ag/AgCl for Mg^{2+}/Mg, La^{3+}/La, and La^{3+} underpotential deposition on a Mg substrate in NaCl−KCl melts, as described in Section 3.1.1, were converted to potentials relative to Cl_2/Cl^-. The results are shown in Table 3. The predicted redox potential of Mg^{2+}/Mg in the NaCl−KCl system exhibited a negative deviation of −0.03 V, while the redox potentials of La^{3+}/La and La^{3+} underpotential

deposition on the Mg substrate showed positive deviations of 0.02 and 0.03 V, respectively. Furthermore, the redox potentials obtained from the DPMD simulations captured the differences between the presence and absence of the Mg substrate in the system, accurately reflecting the underpotential deposition behavior of La^{3+} on the Mg substrate observed during the electrochemical experiments. This outcome confirms the reliability of the DPMD simulation and calculation strategy, while also providing new insights and potential approaches for accurately predicting the redox potentials of metal ions during molten salt electrolysis.

Table 3 Predicted total energy of different systems from DPMD simulations, predictions of redox potentials, and deviation values

System	Total energy/eV	Redox potential by DPMD/V	Redox potential by experiment/V	Deviation/V
Mg-ox	−316.29	−2.60	−2.57	−0.03
Mg-red	−305.10			
La-ox	−294.76	−2.86	−2.88	0.02
La-red	−277.17			
La(Mg)-ox	−295.27	−2.72	−2.75	0.03
La(Mg)-red	−278.12			

3.2.3 Local structure and diffusion coefficient

To gain insight into the microstructural properties of the NKML system, the number of ions in the Mg-ox state, as simulated by AIMD, was increased by 10-fold. The trajectory of the NVT ensemble was analyzed to determine the temporal evolution of RDF, coordination number, and mean square displacement (MSD), as shown in Fig. 11. The first peak of Mg−Cl is higher than that of La−Cl, which is due to the stronger interaction in Mg−Cl pairs, while coordination number of La−Cl (n_{La-Cl}) is higher than that of Mg−Cl (n_{Mg-Cl}).

The diffusion coefficients (D) of Mg^{2+} and La^{3+} in the NKML melts were derived from the evolution of the MSD over time, yielding $D_{Mg^{2+}}=2.82\times10^{-5}$ cm^2/s and $D_{La^{3+}}=1.58\times10^{-5}$ cm^2/s, which closely match the results obtained using the CA technique. Additionally, LIU et al [32] and VANDARKUZHALI et al [33] reported the diffusion coefficients of Mg^{2+} and La^{3+} at different temperatures in LiCl−KCl molten salt, determining that $D_{Mg^{2+}}$ and $D_{La^{3+}}$ at 973 K were 3.67×10^{-5} and 2.78×10^{-5} cm^2/s, respectively. Overall, our experimental and simulation results are in good agreement with the values reported in the literature [32,33]. In the NKML system, Mg^{2+} exhibits a larger diffusion coefficient due to its lower valence state, making it less affected by Coulomb forces during the movement compared to La^{3+}. Moreover, the coordination number of the first shell of Mg−Cl is much smaller than that of La−Cl, meaning that Mg^{2+} encounters less spatial resistance during the movement.

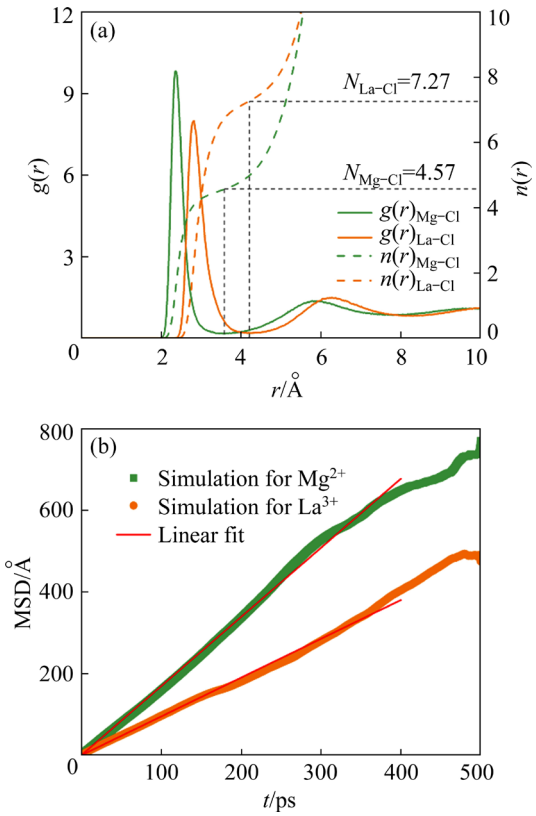

Fig. 11 Local structure information (a) and evolution of MSD with time (b) for NKML melts at 973 K

3.3 Electrolysis and Mg−La alloy characterization

3.3.1 XRD pattern of Mg−La alloys

To obtain the electrolysis products, the concentrations of $MgCl_2$ and $LaCl_3$ in the electrolyte system were increased, resulting in the selection of NaCl−KCl−5wt.%$MgCl_2$−3wt.%$LaCl_3$ mixed salt to produce the Mg−La alloy. Based on the CV results for this system (Fig. 12) and the electrolysis strategy for Mg−Nd alloys [22], potentiostatic electrolysis was performed at −2.30 V on a tungsten electrode (S=0.322 cm^2) at 973 K for

10 h. Figure 13 shows the XRD analysis of the cathodic deposits, which were identified as Mg and $Mg_{17}La_2$.

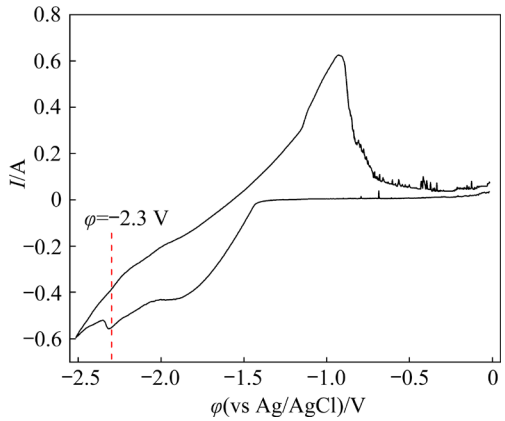

Fig. 12 CV result for NaCl−KCl−5wt.% $MgCl_2$−3wt.% $LaCl_3$ melts at 973 K with scan rate of 0.1 V/s

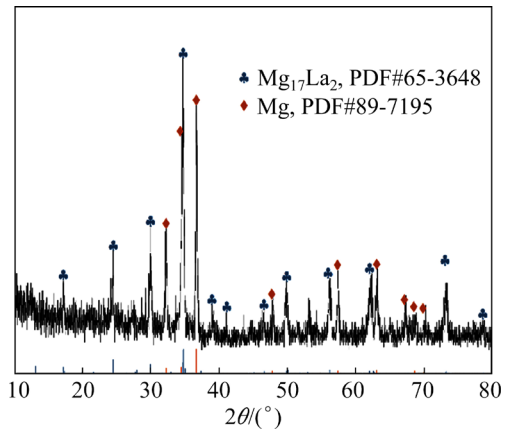

Fig. 13 XRD patterns of cathodic deposits obtained by potentiostatic electrolysis

In the electrochemical experiments, Mg_3La and MgLa were identified in the phase diagrams of Mg−La binary alloys, but these phases did not appear in the final alloy products. TAKENAKA et al [12] demonstrated that the La content in Mg−La alloys prepared by direct electrodeposition in NKML melts depended on the concentration of La^{3+}. The higher Mg^{2+} concentration during electrolysis resulted in the cathodic product being the Mg-rich $Mg_{17}La_2$ phase.

3.3.2 Microstructural characteristics of Mg−La alloy

The microscopic morphologies of the cathodic products were analyzed to understand the electro-reduction mechanism of the Mg−La alloy in the NKML melts. Surface (superficial) and cross-sectional (deep) samples of the cathodic deposits were prepared by controlling the depth of different sections. Figures 14(a), (b), and (c) show the microscopic morphology of the surface samples at different magnifications. Overall, the samples exhibit two distinct phases: a light phase and a dark phase. The light phase forms a dense and irregular network, while the dark phase represents the substrate. Figures 14(d) and (e) show the microscopic morphologies at the edge and center of the cross-sectional sample, respectively. The comparison reveals that the lighter areas are more pronounced in the edge region. Based on subsequent EDS characterization, the dark areas correspond to the Mg phase, while the light areas represent the Mg−La alloy phase. During the electrolysis process, deposition begins at the center

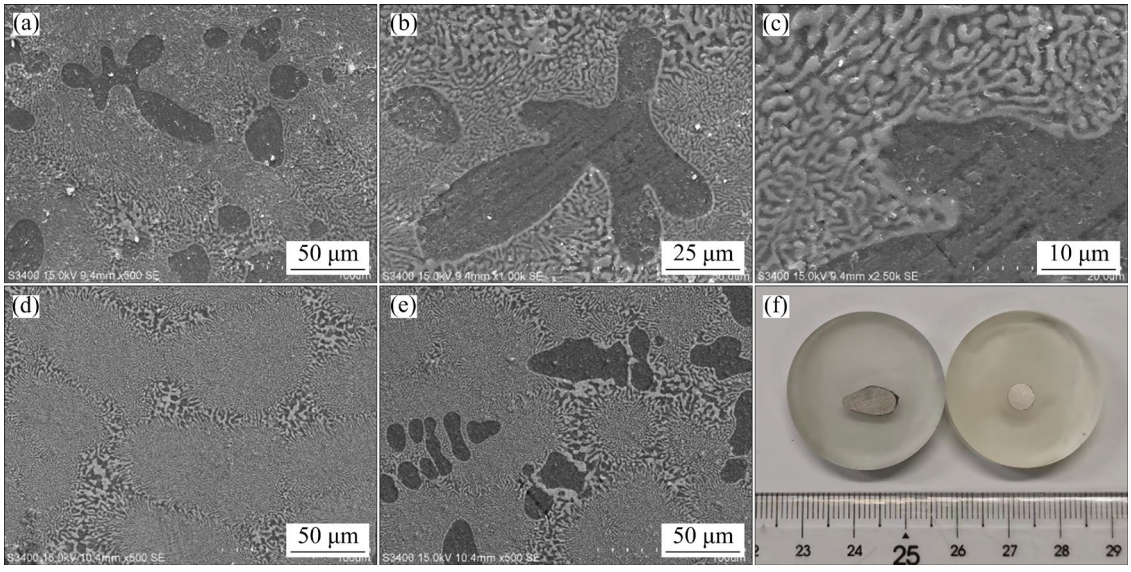

Fig. 14 SEM images of cathodic products (a−e) and sample embedded in epoxy resin (f): (a−c) Microscopic morphologies of surfaces; (d, e) Microscopic morphologies of cross-section at edge and center, respectively

of the sample, followed by the edge region. This indicates that the electrolysis product tends to form the Mg phase in the early stages. As the Mg source in the melt becomes depleted, the product is more likely to transition into the Mg−La alloy phase.

Figure 15 presents the elemental analysis results of the dark and light zones of the electrolysis products. The dark phase contains 95.78 wt.% Mg and 4.22 wt.% O, indicating it corresponds to the Mg substrate, with the presence of O likely due to the oxidation of Mg after polishing. The mass fractions of Mg, La, and O in the light phase are 70.35%, 28.01%, and 1.63%, respectively. The presence of La in the light phase confirms that it corresponds to the Mg−La alloy. Additionally, the introduction of La reduced the mass fraction of O from 4.22% to 1.63%, indicating that the antioxidant properties of Mg alloy with La were improved.

The Mg/La atomic ratio in the bright region is 14.34∶1, which differs from the ratio in the $Mg_{17}La_2$ identified by XRD. This discrepancy is due to the electron beam bombardment during EDS measurements, which results in an averaged elemental ratio over the bombardment depth. The inhomogeneous distribution of the light and dark phases in the vertical direction and the large amount of Mg in the products contribute to a lower La content in the light zones. ICP was subsequently used to determine the total concentration of the samples, yielding Mg and La mass fractions of 85.33% and 14.67%, respectively.

Figure 16 illustrates the element distribution of the electrolysis products analyzed by EDS mappings. Red and green colors represent the elements Mg and La, respectively. In Fig. 16(b), Mg is shown to be distributed throughout the sample, with a higher concentration in the dark phase, as observed in the SEM image. In Fig. 16(c), La is predominantly distributed in the bright zones, which correspond to the Mg−La alloy phase, and is negligible in the dark phase. Figure 16(d) shows the superimposed distribution of Mg and La elements, which aligns with the observations from Figs. 16(b) and (c).

4 Conclusions

(1) The electrochemical experiments in the NKML system demonstrate that the reduction of Mg^{2+} and La^{3+} ions occurs in a single step. The nucleation of Mg and La on the electrode surface follows an instantaneous nucleation mode and is not affected by the alloying process.

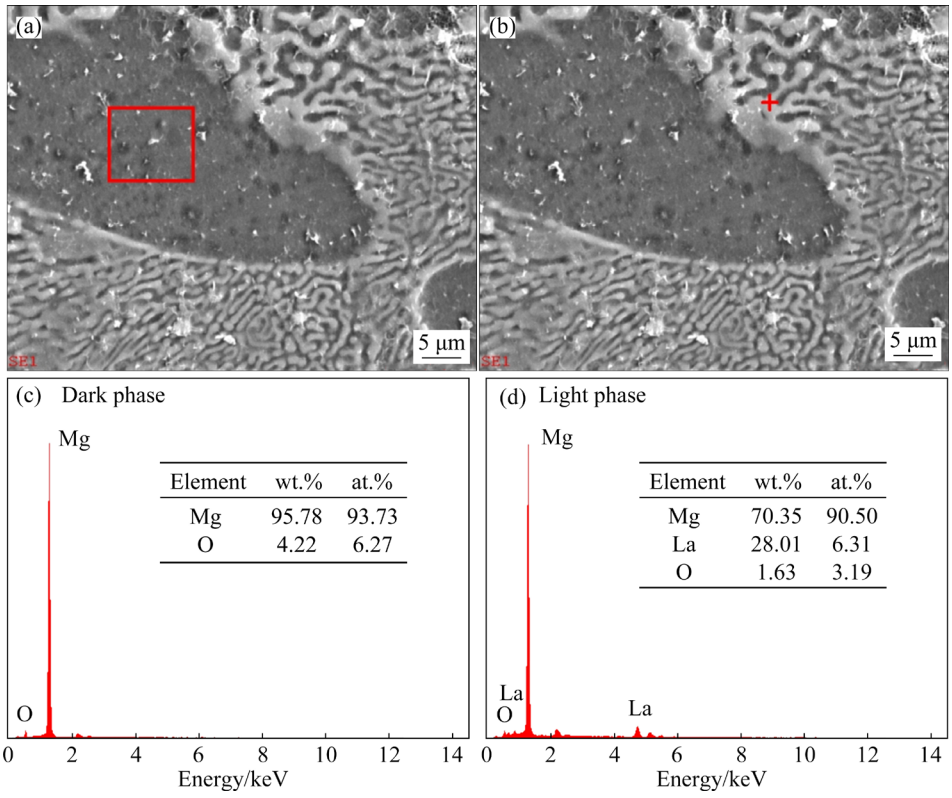

Fig. 15 (a, b) Morphologies of local microzones in cathodic deposit; (c, d) EDS analysis results

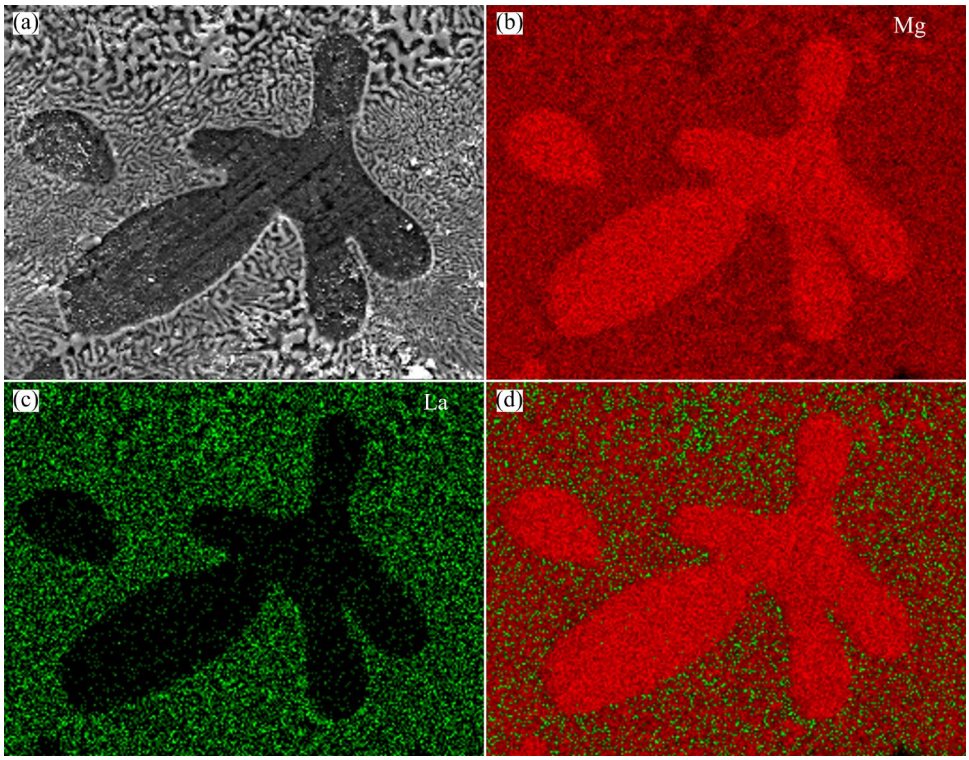

Fig. 16 Elemental distribution of electrolysis products analyzed by EDS mappings: (a) Microscopic morphology; (b, c) Elemental distribution of Mg and La, respectively; (d) Overall distribution of Mg and La

(2) The redox potentials predicted by the trained DP model align well with the experimental values. Furthermore, the redox potential results from the DPMD simulations captured the under-potential deposition behavior of La^{3+} on the Mg substrate, positively influencing the alloying process of Mg−La alloy.

(3) SEM−EDS results confirmed that the cathodic deposits consist of light and dark phases, corresponding to Mg−La alloy and Mg, respectively. Their distribution suggests that the cathodic deposits initially form the Mg phase, with the Mg−La alloy phase emerging later in the alloying process.

CRediT authorship contribution statement

Jia ZHAO: Conceptualization, Methodology, Formal analysis, Writing − Original draft; **Zhi-tao SONG:** Data curation, Visualization, Investigation; **Gui-min LU:** Funding acquisition, Resources, Supervision, Writing − Review & editing.

Declaration of competing interest

The authors declare that they have no known competing financial interests or personal relationships that could have appeared to influence the work reported in this paper.

Acknowledgments

The authors gratefully acknowledge financial support from the National Natural Science Foundation of China (No. U20A20147).

References

[1] XIE Jin-shu, ZHANG Jing-huai, YOU Zi-hao, LIU Shu-juan, GUAN Kai, WU Rui-zhi, WANG Jun, FENG Jing. Towards developing Mg alloys with simultaneously improved strength and corrosion resistance via RE alloying [J]. Journal of Magnesium and Alloys, 2021, 9(1): 41−56.

[2] LIN Jin-ming, FU Peng-huai, WANG Ying-xin, LIU Hong, ZHENG Ya, PENG Li-ming, DING Wen-jiang. Effect of La addition on microstructure, mechanical behavior, strengthening and toughening mechanisms of cast Mg−Gd−Zn alloy [J]. Materials Science and Engineering: A, 2023, 866: 144688.

[3] WANG G G, WEILER J P. Recent developments in high-pressure die-cast magnesium alloys for automotive and future applications [J]. Journal of Magnesium and Alloys, 2023, 11(1): 78−87.

[4] RONG Jian, ZHU Jia-ning, XIAO Wen-long, ZHAO Xin-qing, MA Chao-li. A high pressure die cast magnesium

alloy with superior thermal conductivity and high strength [J]. Intermetallics, 2021, 139: 107350.

[5] LIU Y F, JIA X J, QIAO X G, XU S W, ZHENG M Y. Effect of La content on microstructure, thermal conductivity and mechanical properties of Mg−4Al magnesium alloys [J]. Journal of Alloys and Compounds, 2019, 806: 71−78.

[6] WU Xiao-bin, ZHU Zeng-li, KONG Hui, FAN You-qi, CHENG Si-wei, HUA Zhong-sheng. Electrochemical reduction mechanism of Zn^{2+} in molten NaCl−KCl eutectic [J]. Transactions of Nonferrous Metals Society of China, 2022, 32(9): 3088−3098.

[7] YUAN Rui, LÜ Cheng, WAN He-li, LI Shao-long, CHE Yu-si, HE Ji-lin, SONG Jian-xun. Effect of fluoride addition on electrochemical behaviors of V(III) in molten LiCl−KCl [J]. Transactions of Nonferrous Metals Society of China, 2022, 32(8): 2736−2745.

[8] WANG Z, RAPPLEYE D, YANG C S, SIMPSON M F. Application of voltammetry for electroanalytical measurement of concentrations in $LaCl_3$−$MgCl_2$ mixtures in eutectic LiCl−KCl [J]. Journal of the Electrochemical Society, 2016, 163(10): H921−H926.

[9] JI De-bin, YIN Tai-qi, YAN Yong-de, ZHANG Mi-lin, WANG Pu, LIU Yu-hui, ZHENG Jia-ning, XUE Yun, JING Xiao-yan, HAN Wei. Electrochemical reduction La(III) on W and Mg electrodes: Application to prepare Mg–La and Mg−Li−La alloys in LiCl−KCl melts [J]. RSC Advances, 2016, 6(35): 29353−29364.

[10] SAHOO K D, SINGH H, KRISHNAMURTHY N. Electrochemical deposition of La−Mg alloys in $LaCl_3$−$MgCl_2$−KCl system with molten salt electrolysis process [J]. Journal of Mining and Metallurgy (Section B): Metallurgy, 2014, 50(2): 109−114.

[11] WANG Shi-dong, LI Quan, YE Xiu-shen, SUN Qing-guo, WU Zhi-jian. Electrolytic preparation of Mg−La alloy in chloride molten salt: Effect of electrolyte composition [J]. Rare Metal Materials and Engineering, 2015, 44(7): 1623−1628.

[12] TAKENAKA T, NAKA Y, NARUKAWA N, NOICHI T, KAWAKAMI M. Direct electrodeposition of Mg containing La in molten salt and its corrosion property [J]. Electrochemistry, 2005, 73(8): 706−709.

[13] RODRIGUEZ A, LAM S, HU M. Thermodynamic and transport properties of LiF and FLiBe molten salts with deep learning potentials [J]. ACS Applied Materials & Interfaces, 2021, 13(46): 55367−55379.

[14] XU Ting-rui, LI Xue-jiao, WANG Yang, TANG Zhong-feng. Development of deep potentials of molten $MgCl_2$−NaCl and $MgCl_2$−KCl salts driven by machine learning [J]. ACS Applied Materials & Interfaces, 2023, 15(11): 14184−14195.

[15] ZHAO Jia, WANG Yu-yang, LU Gui-min. Investigation of the redox potential of lithium and its dissolution in the LiCl−KCl eutectic [J]. Journal of the Electrochemical Society, 2022, 169(5): 056517.

[16] ZHAO Jia, FENG Tai-xi, LU Gui-min, YU Jian-guo. Insights into the local structure evolution and thermophysical properties of NaCl−KCl−$MgCl_2$−$LaCl_3$ melt driven by machine learning [J]. Journal of Materials Chemistry A, 2023, 11(44): 23999−24012.

[17] SONG Jia, LI Xue-jiao, SHI Shu-ping, YAN Liu-ming, JIANG Tao, PENG Shu-ming. Towards the calculations of redox potentials in molten LiCl−KCl eutectic by ensemble averages based on first principles molecular dynamics [J]. Electrochimica Acta, 2017, 248: 462−469.

[18] ZHAO Jia, LIANG Wen-shuo, LU Gui-min. Theoretical prediction on the redox potentials of rare-earth ions by deep potentials [J]. Ionics, 2021, 27(5): 2079−2088.

[19] KRESSE G, FURTHMÜLLER J. Efficient iterative schemes for ab initio total-energy calculations using a plane-wave basis set [J]. Physical Review B, 1996, 54(16): 11169−11186.

[20] ZHANG Lin-feng, HAN Jie-qun, WANG Han, CAR R, E Wei-nan. Deep potential molecular dynamics: A scalable model with the accuracy of quantum mechanics [J]. Physical Review Letters, 2018, 120(14): 143001.

[21] PLIMPTON S. Fast parallel algorithms for short-range molecular dynamics [J]. Journal of Computational Physics, 1995, 117(1): 1−19.

[22] HUA Zhong-sheng, LIU Huan, WANG Jian, HE Ji-wen, XIAO Sai-jun, XIAO Yan-ping, YANG Yong-xiang. Electrochemical behavior of neodymium and formation of Mg−Nd alloys in molten chlorides [J]. ACS Sustainable Chemistry & Engineering, 2017, 5(9): 8089−8096.

[23] LI Xing, YAN Yong-de, ZHANG Mi-lin, TANG Hao, JI De-bin, HAN Wei, XUE Yun, ZHANG Zhi-jian. Electrochemical reduction of Tm on Mg electrodes and co-reduction of Mg, Li and Tm on W electrodes [J]. Electrochimica Acta, 2014, 135: 327−335.

[24] MEIER J M, CARIS J, LUO A A. Towards high strength cast Mg−RE based alloys: Phase diagrams and strengthening mechanisms [J]. Journal of Magnesium and Alloys, 2022, 10(6): 1401−1427.

[25] WANG Ying-cai, LIU Qian, ZHANG Shuang, LIU Yu-hui, WANG You-qun, DAI Ying, DONG Zhi-min, CHENG Zhong-ping, CAO Xiao-hong, CHEN Yu-qian, ZHANG Zhi-bin, LIU Yun-hai. Electrolytic extraction of yttrium using recycle liquid gallium electrode from molten LiCl−KCl [J]. Separation and Purification Technology, 2022, 294: 120972.

[26] SCHARIFKER B, HILLS G. Theoretical and experimental studies of multiple nucleation [J]. Electrochimica Acta, 1983, 28(7): 879−889.

[27] LIANG Wen-shuo, LU Gui-min, YU Jian-guo. Theoretical prediction on the local structure and transport properties of molten alkali chlorides by deep potentials [J]. Journal of Materials Science & Technology, 2021, 75: 78−85.

[28] LIANG Wen-shuo, LU Gui-min, YU Jian-guo. Machine learning accelerates molten salt simulations: Thermal conductivity of $MgCl_2$−NaCl eutectic [J]. Advanced Theory and Simulations, 2022, 5(8): 2200206.

[29] LIANG Wen-shuo, LU Gui-min, YU Jian-guo. Machine-learning-driven simulations on microstructure and thermophysical properties of $MgCl_2$−KCl eutectic [J]. ACS Applied Materials & Interfaces, 2021, 13(3): 4034−4042.

[30] FENG Tai-xi, ZHAO Jia, LIANG Wen-shuo, LU Gui-min. Molecular dynamics simulations of lanthanum chloride by deep learning potential [J]. Computational Materials Science, 2022, 210: 111014.

[31] NAM H O, MORGAN D. Redox condition in molten salts and solute behavior: A first-principles molecular dynamics study [J]. Journal of Nuclear Materials, 2015, 465: 224−235.
[32] LIU Zhao-ting, LU Gui-min, YU Jian-guo. Investigation on electrochemical behaviors of $MgCl_2$ impurity in LiCl−KCl melt [J]. Journal of Electroanalytical Chemistry, 2021, 886: 115131.
[33] VANDARKUZHALI S, GOGOI N, GHOSH S, PRABHAKARA REDDY B, NAGARAJAN K. Electrochemical behaviour of $LaCl_3$ at tungsten and aluminium cathodes in LiCl−KCl eutectic melt [J]. Electrochimica Acta, 2012, 59: 245−255.

NaCl−KCl−$MgCl_2$−$LaCl_3$ 熔体中 Mg−La 的合金化过程

赵 佳[1,2]，宋智涛[1,2]，路贵民[1,2]

1. 华东理工大学 国家盐湖资源综合利用工程技术研究中心，上海 200237；
2. 华东理工大学 钾锂战略资源国际联合实验室，上海 200237

摘 要：采用电化学技术和深度势能分子动力学(DPMD)模拟研究了 NaCl−KCl−$MgCl_2$−$LaCl_3$(NKML)熔体在电还原过程中 Mg−La 的合金化过程。973 K 时，NKML 熔体中 Mg^{2+}/La^{3+}在 W 电极上的电沉积为一步过程，金属离子在电极表面的成核方式为瞬时成核且不受合金化过程的影响。利用 DPMD 模拟，准确预测了 NKML 熔体中金属离子的氧化还原电位和欠电位沉积行为，证实了 Mg−La 的合金化过程。此外，SEM−EDS 的分析结果显示，阴极沉积产物 Mg−La 和 Mg 分别表现为明和暗两相。电解产物分布表明，电解早期容易形成 Mg 相，随着熔体中 Mg 被消耗，电解产物更易形成 Mg−La 合金相。

关键词：NaCl−KCl−$MgCl_2$−$LaCl_3$ 熔体；Mg−La 合金；合金化过程；电还原；氧化还原电位

(Edited by Wei-ping CHEN)